nature communications

Article

https://doi.org/10.1038/s41467-025-55838-6

Designer topological-single-atom catalysts with site-specific selectivity

Received: 15 May 2024

Accepted: 26 December 2024

Published online: 10 January 2025

Check for updates

Weibin Chen[1,2], Menghui Bao[3], Fanqi Meng[1], Bingbing Ma[1], Long Feng[3], Xuan Zhang[1], Zanlin Qiu[1], Song Gao[1], Ruiqin Zhong[3], Shibo Xi[4], Xiao Hai[1] ✉, Jiong Lu[5] ✉ & Ruqiang Zou[1,6] ✉

Designing catalysts with well-defined, identical sites that achieve site-specific selectivity, and activity remains a significant challenge. In this work, we introduce a design principle of topological-single-atom catalysts (T-SACs) guided by density functional theory (DFT) and Ab initio molecular dynamics (AIMD) calculations, where metal single atoms are arranged in asymmetric configurations that electronic shield topologically misorients *d* orbitals, minimizing unwanted interactions between reactants and the support surface. Mn_1/CeO_2 catalysts, synthesized via a charge-transfer-driven approach, demonstrate superior catalytic activity and selectivity for NO_x removal. A life-cycle assessment (LCA) reveals that Mn_1/CeO_2 significantly reduces environmental impact compared to traditional V-W-Ti catalysts. Through in-situ spectroscopic characterizations combined with DFT calculations, we elucidate detailed reaction mechanisms. This study establishes T-SACs as a promising class of catalysts, offering a systematic framework to address catalytic challenges by defining site characteristics. The concept highlights their potential for advancing selective catalytic processes and promoting sustainable technologies.

The contemporary focus in the field of catalysis is centered on the ability to achieve precise selectivity while maintaining, or even enhancing, high catalytic activity[1–4]. As catalytic systems and their objectives have grown more complex, the difficulty in selectively promoting desired reactions while suppressing undesired ones has significantly increased[1]. For instance, in the selective catalytic reduction of nitrogen oxides (NO_x) using ammonia (NH_3-SCR)[5,6], the challenge lies in oxidizing NH_3 to NH_2 without further overoxidizing it to NH species. The overoxidation of NH_3 can lead to the production of N_2O instead of the desired N_2[7,8], which is problematic since N_2O has approximately 300 times the global warming potential (GWP) of CO_2 over a 100-year period[9]. Similarly, when dealing with organic molecules with multiple unsaturated bonds, selectively hydrogenating one bond without affecting others is a significant hurdle[10–12]. A key strategy for controlling reaction selectivity involves designing catalysts that exhibit specific-sites tailored to form the desired products[13–15]. This often requires exploiting or modifying the steric and electronic properties of these active sites[16,17]. Despite significant advances[18–23], the intricate interactions between catalytic sites and substrates are often discovered by chance, making them difficult to predict or systematically apply across different systems[24].

Heterogeneous single-atom catalysts (SACs)[25–27], featuring well-defined mononuclear metal sites with tunable coordination and configuration on a support material, present a promising solution to these challenges[28–30]. The isolation of metal atoms in SACs allows for the precise design of active centers guided by theoretical principles[31–34].

[1]School of Materials Science and Engineering, Peking University, Beijing, P.R. China. [2]Department of Nuclear Science and Engineering, Massachusetts Institute of Technology, Cambridge, MA, USA. [3]State Key Laboratory of Heavy Oil Processing, China University of Petroleum, Beijing, P.R. China. [4]Institute of Sustainability for Chemicals, Energy and Environment (ISCE2), Agency for Science, Technology and Research (A*STAR), Singapore, Singapore. [5]Department of Chemistry, National University of Singapore, Singapore, Singapore. [6]School of Advanced Materials, Peking University Shenzhen Graduate School, Shenzhen, P.R. China. ✉e-mail: xiaohai@pku.edu.cn; chmluj@nus.edu.sg; rzou@pku.edu.cn

While previous studies[35–37] have made significant progress in designing "embedded Pt" and "adsorbed Pt" catalysts by focusing on single-atom design through geometric structures or analogies to doped/substituted surface structures, these approaches have not fully achieved the precise site-specific design from the perspectives of crystal field design or orbital symmetry. In this work, we introduce a novel design principle for topological-single-atom catalysts (T-SACs) that target site-selective reactions. In these catalysts, reactants temporarily bond with topologically arranged single atoms, allowing for precise control over reaction sites. We demonstrate this concept using the NH_3-SCR reaction as a model system.

To date, Mn single-atom moieties prepared through scalable methods that simultaneously achieve high activity and excellent selectivity in NH_3-SCR reactions have not been reported. Through density functional theory (DFT) and Ab initio molecular dynamics (AIMD) calculations we demonstrate that the designed Mn_1/CeO_2 single-atom moiety effectively stabilizes adsorbates and critical intermediates, thereby enhancing reaction performance. The metal single atoms, arranged in asymmetric configurations, utilize electronic *d* orbital shielding and spatial hindrance to protect the support surface from direct interactions with reactants. As a proof of concept, Mn_1/CeO_2 were synthesized using a charge-transfer-driven approach, which is readily scalable to kilogram-scale production and is characterized by low energy consumption, minimal environmental impact, and reduced costs. Catalytic evaluation of NH_3-SCR shows that Mn_1/CeO_2 exhibit exceptional performance compared to both manganese oxides and other benchmark catalysts. An ex-ante Life Cycle Assessment (LCA) quantifying the environmental benefits of the Mn_1/CeO_2 over traditional V-W-Ti catalyst shows a much lower carbon footprint in four recognized metrics. In-situ characterization and theoretical studies unravel the complete reaction pathway of NH_3-SCR over Mn_1/CeO_2. This study shows that Mn_1/CeO_2 surmounts the long-standing challenge of striking a delicate equilibrium SCR activity and N_2 selectivity at low temperatures, underscoring the immense potential of this new class of SCR catalysts at the forefront of next-generation NO_x removal technology. Furthermore, the concept of T-SACs offers broad potential for application in the selective processing of various reactants and catalytic processes, with opportunities for further generalization using alternative supports, single atoms, and electronic structures.

Results

Definition of topological-single-atom catalysts

T-SACs feature metal single atoms arranged in distinctive, asymmetric configurations that, through their spatial and electronic topological structure, effectively shield the support surface from direct interaction with reactants linked to these atoms (Fig. 1). The catalytic behavior of T-SACs mirrors that of topology-defined conductive surface states, in contrast to the insulating bulk states in a topological insulator. Similar to electrons confined to moving along the surface of the material in a topological insulator, the design of T-SACs ensures that only the protruding metal single atoms actively engage in reactions, thus improving the selectivity of a designated catalytic process. This design principle relies on precise spatial arrangement enabled electronic shielding of mis-oriented *d* orbitals to restrict the interaction of reactive substrates with the bulk of the catalyst. Such a design effectively reduces the likelihood of side reactions that could diminish the yield of the desired product. Additionally, the symmetry breaking in the crystal field lead to a partial *d* electron shielding of T-SACs allows for precise control of reaction pathways, making these materials particularly advantageous for applications in site-specific catalysis, where catalyst specificity can significantly impact the purity and functionality of the end products.

For example, low-temperature NH_3-SCR reactions represent the next generation of low-energy consumption denitrification technology aimed at addressing the harm to sustainable development caused by NO_x emissions[5,6,38–42] (Fig. S1). MnO_x complexes serve as effective catalysts in low temperature NH_3-SCR reactions due to the ability of their Mn active sites to readily activate N-H bonds in NH_3[8,43]. However, the peroxidation of NH_3 often results in the unwanted production of N_2O, a by-product that reduces the selectivity for N_2 (Fig. S2). The over-dissociation of NH_2 on the catalyst surfaces primarily stems from an abundance of oxygen atoms, with the unsaturated oxygen atoms on the MnO_x surface engaging with the hydrogen atoms in NH_2 (Fig. S3). Through the constrained AIMD simulations, the dissociation process of NH_2^* on the MnO_x surface was elucidated (Fig. S4c–f), revealing that NH_2^* can be easily split into NH^* and OH^* under the influence of surface oxygen atoms. This decomposition, particularly the formation of NH^*, can contribute to the generation of the by-product N_2O. It is therefore imperative to design novel Mn single-atom moieties that are fundamentally distinct from conventional MnO_x, Mn-doped CeO_2, $MnCeO_x$, or MnO_x/CeO_2, to effectively mitigate NH_3 peroxidation.

Topological design of Mn_1/CeO_2 catalyst for selective NO_x removal

Grounded in theoretical insights, a novel Mn single-atom catalyst (Mn_1/CeO_2) featuring a distinctive tetrahedral coordination structure was designed to prevent adsorbed NH_2^* from being overwhelmed by surrounding oxygen atoms (Fig. 1b). The elevated positioning of the Mn single atoms creates a spatial buffer between NH_2^* and the substrate O atoms, which significantly hinders the dissociation of NH_2^*, a finding confirmed by AIMD simulations. Specifically, the energy barrier for NH_2^* dissociation on the Mn_1/CeO_2 surface is notably higher than 1.57 eV (Fig. S4b), presenting a stark contrast to the lower energy barriers encountered on various manganese oxide surfaces (Fig. S4, 0.63 eV for MnO, 0.61 eV for Mn_2O_3, 0.97 eV for Mn_3O_4, and 0.66 eV for MnO_2). These results are further supported by climbing image nudged-elastic band (CINEB) calculations (Fig. S5), highlighting the energetic advantage of the topological Mn_1/CeO_2 in preventing the dissociation of NH_2^*.

The Walsh diagram for NH_2 molecular orbitals ($2a_1^2\,1b_2^2\,3a_1^2\,1b_1^1$) is shown in Fig. S6a. Following such knowledge, it is clear that electron transfer from Mn to NH_2 can result in its activation; therefore, weak bonding between Mn and NH_2 is demanding to suppress further oxidation. The intricate interaction between the Mn atom and adsorbed NH_2^* is explored through analyses of the σ and π bonds and their anti-bonding counterparts (Fig. S6b). Given the fundamental difference between MnO and Mn_1/CeO_2, which is the change in local coordination, crystal field theory has been employed to evaluate the Mn-N interaction. The analysis extends to the projected density of states (DOS), revealing notable spin polarization among these catalysts, dominated by spin-up states (Fig. S7), as closely examined in the orbital overview presented in Figs. 1c and S7. Specifically, MnO catalyst presents with six-coordinated Mn (Mn-L6) and leads to distorted octahedral field with spin up states, according to which several electrons fill in anti-bonding states (π^*, $2e_g$). Accordingly, strong Mn-NH_2 interaction origins from σ and π bonds (see Fig. S8a). Such picture has been confirmed by calculated Crystal Orbital Hamilton Population (COHP) profile (Fig. S7), from which an integrated bond order index (ICOBI) of 0.58 has been obtained. Clearly, to suppress NH_2→NH conversion, it is highly essential to weaken Mn-N interaction, which can be achieved via the breaking of octahedral symmetry. Our strategy is to protect a part of Mn 3*d* orbitals by topological shielding through changing Mn-L6 to Mn-L4 as demonstrated by Mn_1/CeO_2. In this case, Mn 3*d* splits into $E + T_2$, while *E* orbitals ($d_{x^2-y^2}$, d_{z^2}) can hardly interact with the ligands due to the symmetry mismatch (Fig. 1c). As a result, the interaction between Mn and N is significantly reduced, as evidenced by a lower ICOBI value of 0.23, leading to a higher energy barrier for NH^* formation (1.58 eV) compared to that over MnO (0.63 eV). Additionally, the Mn_1/CeO_2 configuration shows the weakest Mn-NH_2 interaction compared to other crystal-field manganese oxides

https://doi.org/10.1038/s41467-025-55838-6

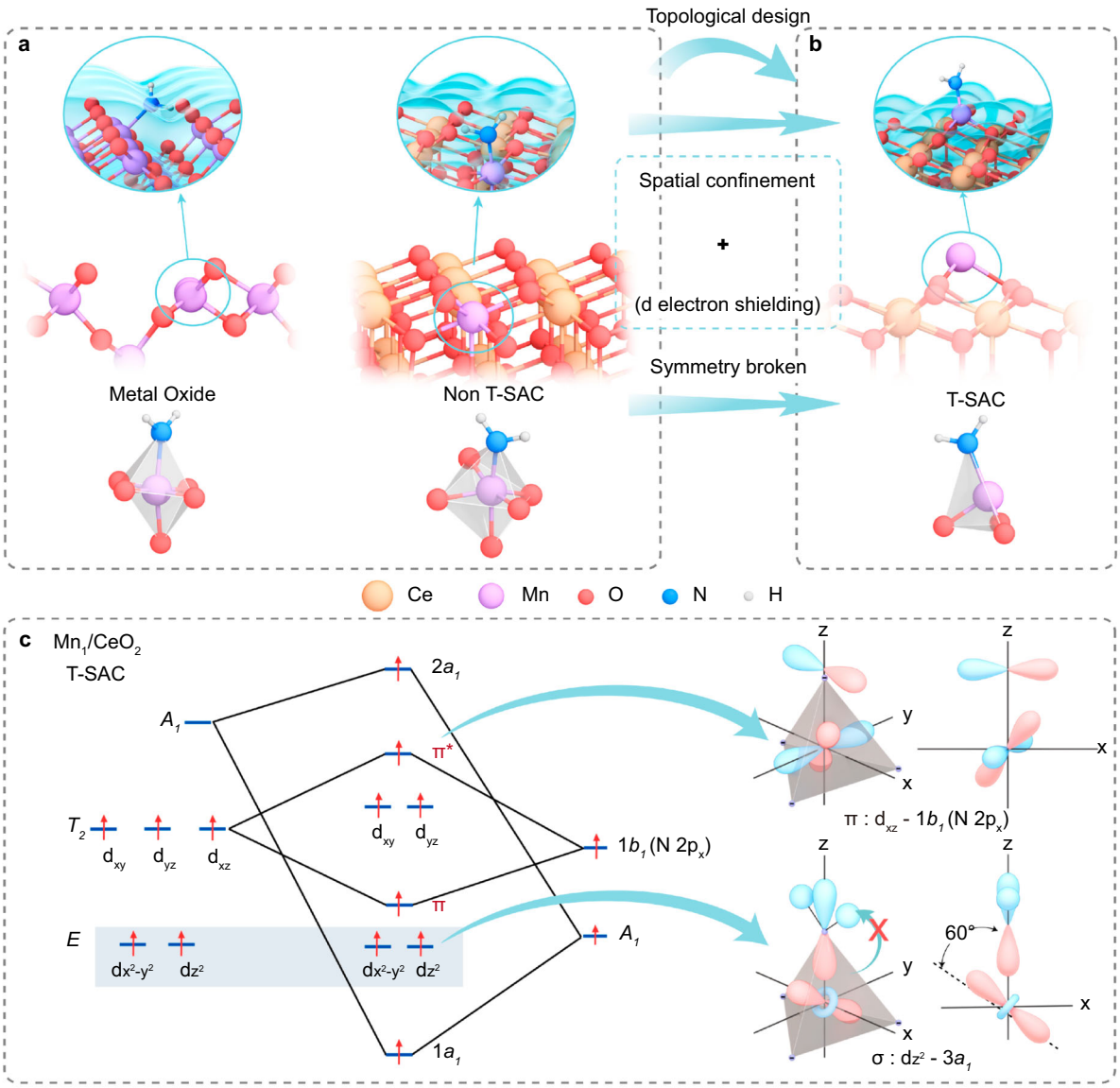

Fig. 1 | Design principles of T-SACs. a, **b** Conceptual framework of T-SACs: Single atoms are strategically positioned in spatially distinct and asymmetric configurations, which, within their electronic structure, act to shield the support from direct interaction with reactants attached to these metal atoms. This arrangement is complemented by the crystal field environment of topologically designed metal sites, achieving precise activation of reactants through symmetry broken. **c** Orbital interaction of Mn-NH_2 in Mn-L4 coordination and Mn-N σ and π bonding over Mn_1/CeO_2. Mn 3*d* splitting is associated with Mn-L4 tetrahedral field in Mn_1/CeO_2. Colour code: Nitrogen, blue; Oxygen, red; Hydrogen, white; Cerium, yellow; Manganese, purple.

(such as ML5's Mn_3O_4, see Fig. S9), fully demonstrating its superiority in effectively inhibiting the peroxidation reaction of NH_2 and promoting NO removal (see Fig. S3b).

Large-scale synthesis and characterization

Given the difficulty in loading metal single atoms on a support, a charge-transfer-driven approach was devised for the synthesis of Mn_1/CeO_2. The cornerstone of this approach is the controlled removal of ligands from metal precursors and the careful management of their interactions with the support. For Mn_1/CeO_2, the key advancement involves the gradient decomposition of citric acid (CA) complexes, selectively targeting the support and single atomic elements. Initially, a mixed solution of MnCA and CeCA was prepared (Fig. 2a), ensuring homogeneity, as confirmed by the TEM and EDS images of the MnCA + CeCA precursor obtained after solvent evaporation (Figs. 2b and S10). The precursor underwent an initial annealing at 150 °C, which initiated the decomposition of CeCA into CeO_2, forming CeO_2 supports with (111) surfaces while avoiding the decomposition of MnCA. As depicted in Figs. 2c and S11, this process results in an amorphous layered structure corresponding to undecomposed MnCA and nanoparticles representing CeO_2. Subsequently, a series of ball milling processes was conducted alongside a second annealing at 250 °C. During this stage, spontaneous charge transfer from the CA ligand to the support facilitated the kinetic migration and thermal stabilization of the Mn single atoms (further detailed in the AIMD analysis in the next section). Finally, the MnCA + CeO_2 precursor underwent a final annealing to remove the remaining ligands from

https://doi.org/10.1038/s41467-025-55838-6

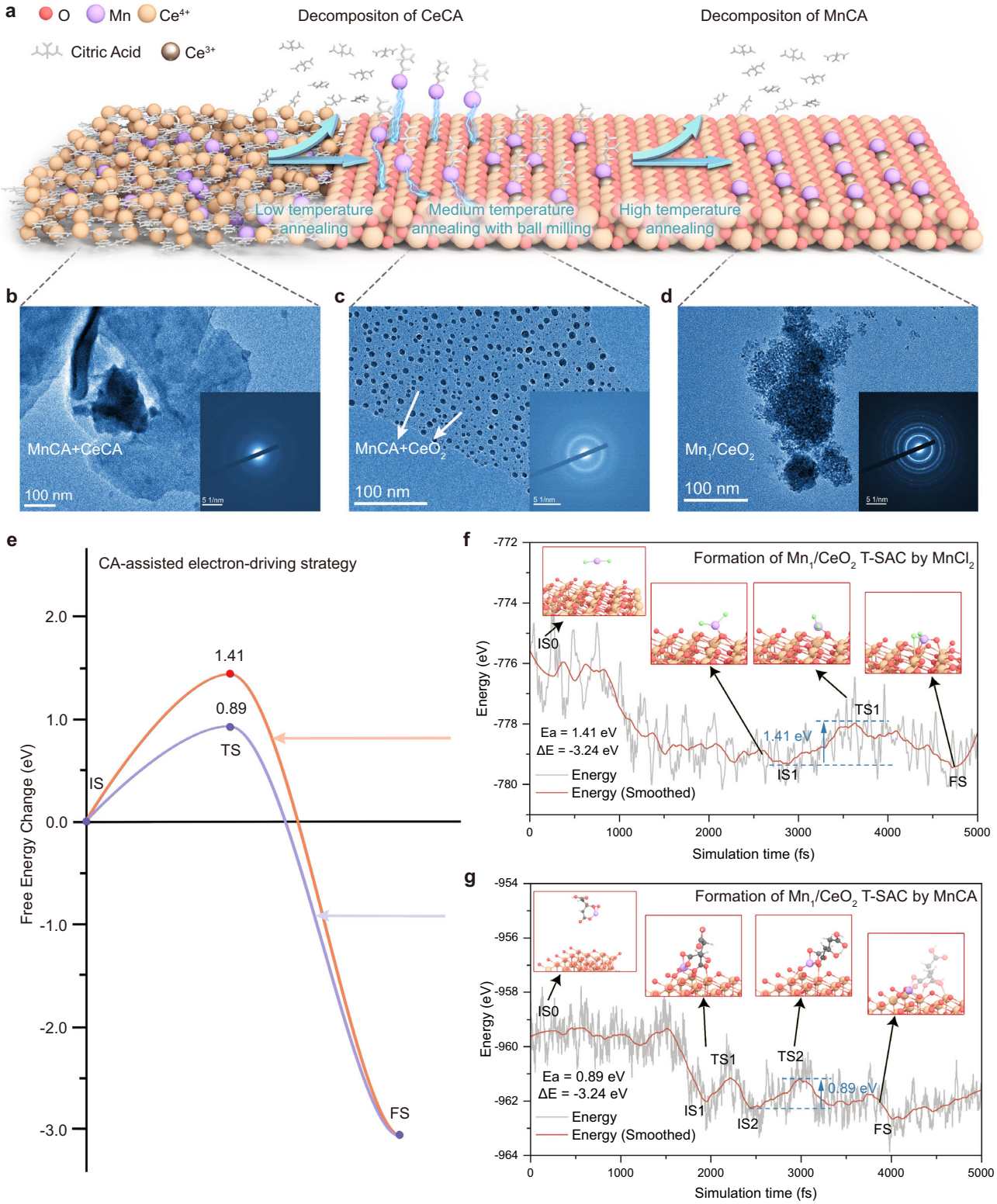

Fig. 2 | Large-scale synthesis and characterization of Mn_1/CeO_2. a Strategy for the preparation of Mn_1/CeO_2. **b**–**d** TEM images of different states of the synthesis process. **e**–**g** The difference in energy barriers (**e**) for the anchoring of Mn single atoms on the CeO_2 surface with the use of MnCA (**f**) and $MnCl_2$ (**g**) as metal precursors, respectively.

the Mn atoms, stabilizing them on the CeO_2 lattice and resulting in the formation of Mn_1/CeO_2. The TEM and EDS surface scanning images in Fig. 2d and Fig. S12 confirm the complete decomposition of MnCA and CeCA, as evidenced by the presence of CeO_2 nanoparticles without any amorphous precursor layers and the uniform distribution of Mn and Ce elements.

AIMD simulations were then employed to elucidate the critical stages in the synthesis of Mn_1/CeO_2 (Fig. 2e). Our theoretical analysis revealed that employing MnCA as a metal precursor (Fig. 2g) can effectively reduce the kinetic barrier for the anchoring of Mn single atoms onto CeO_2 surface, reducing it from 1.41 eV to 0.89 eV, in comparation to conventional compounds like $MnCl_2$ (Fig. 2f). The

reduction in the energy barrier is primarily attributed to the weak bonding interaction between the oxygen atoms in CA and the cerium atoms in CeO_2. As MnCA approaches the CeO_2 surface, the spontaneous charge transfer from the CA ligand to the support simultaneously assists in the kinetic migration and thermal stabilization of the Mn single atoms. Fig. S13 illustrates that as the temperature increases, the CA component in MnCA progressively decomposes, while the single Mn atoms continue to be firmly anchored within the pockets formed by three oxygen atoms on CeO_2. Moreover, stability simulations conducted in SCR reaction (Fig. S14) demonstrated that the single Mn atoms remain highly stable and do not aggregate under the harsh conditions.

The existence of Mn atoms on the surface as single atoms with a distinctive tetrahedral coordination structure was verified through multiple advanced characterization techniques. X-ray diffraction (XRD) patterns of Mn_1/CeO_2 showed only diffraction peaks characteristic of the cubic fluorite structure of CeO_2 (Fig. 3a, b and Table S1). No lattice distortion was detected in the CeO_2 support, even with the incorporation of a high Mn content exceeding 3 wt% (Table S2), ruling out the possibility of Mn doping or Mn-Ce solid solution formation. The annular dark-field scanning transmission electron microscopy (ADF-STEM) images revealed bright spots approximately 0.2 nm in diameter, which correspond to Mn atoms superimposed on the CeO_2 surface (Figs. 3c and S15). This observation is in good alignment with the simulated atomic structure of Mn on the (111) surface of CeO_2. The presence of single Mn atoms was further confirmed by atomic-scale electron energy loss spectroscopy (EELS) and elemental mapping of Mn_1/CeO_2 (Fig. 3d), where a pronounced Mn L-edge signal was observed at the corresponding position. Large-scale energy-dispersive X-ray spectroscopy (EDS) elemental mapping verified the uniform distribution of Mn, with only CeO_2-related lattice structures observed (Fig. S16).

X-ray absorption near-edge structure (XANES) spectra indicated that the Mn sites in Mn_1/CeO_2 are in a positive oxidation state (Fig. S17a). Fourier-transformed extended X-ray absorption fine structure (EXAFS) spectra (Figs. 3f and S17b) and wavelet-transformed EXAFS (Fig. S17c–h) confirmed the presence of Mn single-atom metal sites. Only a strong first-shell M-O peak was observed, corresponding to the Mn-O scattering pathway, with no evidence of a first-shell Mn-Mn peak. After fitting the EXAFS spectrum (Fig. S18), the specific fitting parameters, summarized in Table S3, revealed that the Mn-O coordination number and bond length closely align with the topological design. To further confirm the atomic configuration of the Mn sites, first-principles calculations were performed to explore potential models and simulate their corresponding XANES spectra. The model proposing a tetrahedral structure of a single Mn atom stabilized by four oxygen atoms on the CeO_2 (111) surface showed the closest match with the experimental Mn K-edge XANES spectrum (Fig. 3e). Although there are minor discrepancies between the model and experimental data, the key criterion for validating a model is that the positions of the features in both the simulated and experimental spectra closely correspond. These results conclusively demonstrate that single Mn atoms are robustly stabilized on the top surface of the CeO_2 support in a topologically tetrahedral configuration. In addition, it is worth emphasizing that the synthetic approach presented in this study offers a versatile and scalable method for preparing T-SACs beyond Mn. By preciously controlling the annealing temperature and further optimizing the process (Table S4), as determined by the thermogravimetric analysis (TGA) of the corresponding precursors (Fig. S19), we successfully synthesized catalysts with other metals supported on CeO_2. The presence of these metals in single atom form was confirmed through XANES spectra, FT-EXAFS, WT-EXAFS, and EXAFS fitting (Fig. S20, Table S5 for Fe; Fig. S21, Table S6 for Ru; Fig. S22, Table S7 for Zn). Most importantly, this approach can be readily scaled up to produce quantities in the tens of kilograms, representing a significant milestone toward industrial implementation (see Fig. S23). In contrast, if the carefully planned multi-step ligand removal process and the charge transfer from the MnCA ligand to the support are bypassed, and the MnCe mixed precursor is instead subjected to a single high-temperature calcination, MnO_x/CeO_2 catalysts are formed. This is clearly shown by the Rietveld-refined X-ray diffraction patterns, which reveal distinct peaks corresponding to Mn_2O_3 and Mn_3O_4 phases, as seen in Fig. S24 and detailed in Table S8.

Catalytic performance of Mn_1/CeO_2

To demonstrate that the newly designed Mn_1/CeO_2 catalyst exhibits fundamentally different behavior from conventional Mn-based catalysts, we evaluated its catalytic performance in NH_3 oxidation and NH_3-SCR reactions. As shown in Fig. S25, we employed a systematic selection of control catalysts to ensure comprehensive and rigorous comparisons. These included Mn oxides with varying oxidation states, such as MnO_2, Mn_3O_4, Mn_2O_3, and MnO, as well as several commonly used Mn-Ce-based catalysts, such as Mn-doped CeO_2, MnO_x/CeO_2, and $MnCeO_x$ (additional synthesis and characterization details provided in Supplementary Note 1, Fig. S26–S38 and Table S9). Specifically, evidence for the proper formation of octahedral Mn sites in $MnCeO_x$ and MnO_x catalysts can be found in Supplementary Note 2, Figs. S39 and S40 and Table S10. To confirm that the catalytic performance originates from the Mn active sites rather than the CeO_2 support, we also synthesized pure CeO_2 without incorporating the Mn precursor. Additionally, we synthesized the traditional V-W-Ti catalyst to further explore the commercial potential of Mn_1/CeO_2.

We first assessed the adsorption and oxidation capabilities of NH_3 and NO on Mn_1/CeO_2. The NH_3-TPD analysis (Fig. 4a) displayed desorption peaks at 300 °C, 400 °C, and 700 °C for the Mn_1/CeO_2, with a peak area considerably larger than that of the CeO_2 samples. This indicates that the incorporation of single Mn atoms greatly enhances the catalyst's NH_3 adsorption capacity. Figure 4b shows that the onset temperature for NH_3 oxidation decreased from 240 °C for CeO_2 to 150 °C for Mn_1/CeO_2, demonstrating improved NH_3 oxidation activity due to the addition of Mn single atoms. However, for MnO_x/CeO_2 catalysts, NH_3 overoxidation was observed, with the NH_3 oxidation rate exceeding 60% between 150 °C and 270 °C, leading to reduced selectivity. The NO oxidation ability of Mn_1/CeO_2 showed no significant enhancement (Fig. 4c), indicating that the fast-SCR pathway contributes minimally to the overall catalytic activity and selectivity of Mn_1/CeO_2.

For the NH_3-SCR performance evaluation, we initially conducted tests in the absence of SO_2 and H_2O to effectively assess the intrinsic catalytic capabilities of the Mn_1/CeO_2 (Fig. 4d–f). Following this, we introduced SO_2 and H_2O to the reaction environment to evaluate the catalysts' resistance to poisoning and their overall stability, which are crucial for commercial applications (Fig. 4g–h). Figure 4d–e present the NO conversion and N_2 selectivity as functions of temperature. Notably, the incorporation of a single Mn atom into CeO_2 led to a increase in NO conversion from 4% to an impressive 99% at a low reaction temperature of 90 °C. This modification extended the effective denitrification temperature range to 90–240 °C, maintaining SCR activity above 95% while achieving consistently high N_2 selectivity, remaining above 90% throughout this temperature range. This performance significantly surpasses that of all other catalysts tested. Although MnO_x/CeO_2 catalysts achieved NO conversion rates comparable to Mn_1/CeO_2, Fig. 4e indicates a marked decline in N_2 selectivity for MnO_x/CeO_2 catalysts as temperature increased, dropping below 20% at 240 °C. Similarly, the N_2 selectivity of other MnO_x catalysts (MnO_2, Mn_3O_4, Mn_2O_3, and MnO) also fell below 20% at 240 °C. The sharp rise in N_2O production for MnO_x and MnO_x/CeO_2 catalysts with increasing temperature, exceeding 300 ppm at 210 °C (Fig. 4f), provides direct evidence of this limitation. In contrast, Mn_1/CeO_2

https://doi.org/10.1038/s41467-025-55838-6

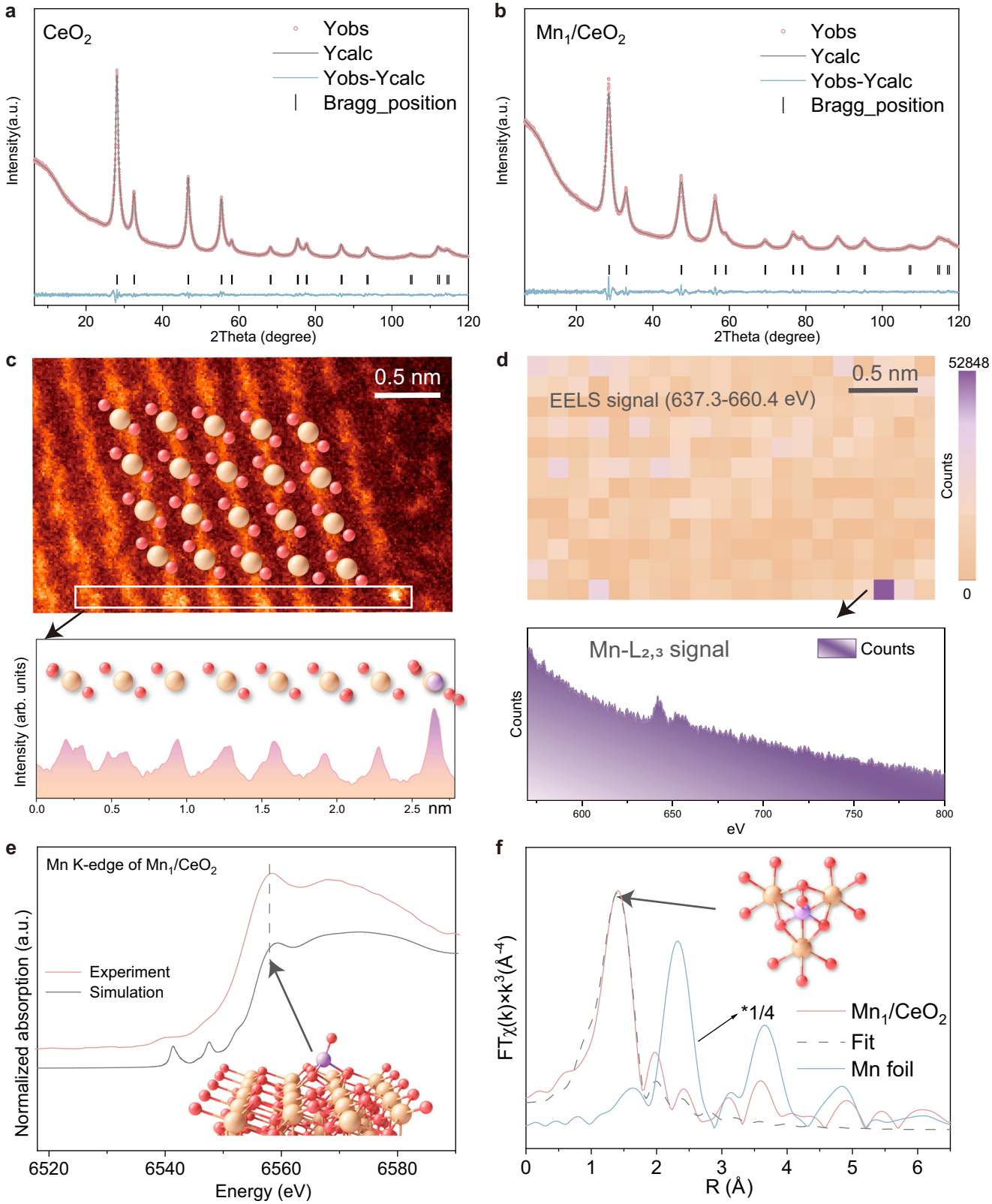

Fig. 3 | Characterization of Mn_1/CeO_2. **a**, **b** Rietveld refined X-ray diffraction patterns for the CeO_2, Mn_1/CeO_2. a. u. arbitrary units. **c** Atomic-resolution AC-HAADF-STEM image of Mn_1/CeO_2 containing single Mn atoms. **d** Electron energy loss spectroscopy (EELS) analysis for (**c**) in Mn_1/CeO_2. **e** The experimental high-resolution XANES spectrum compared with the calculated XANES data of optimized DFT-modelled structure of Mn_1/CeO_2. a. u. arbitrary units. **f** K_3-weighted Mn K-edge Fourier-transformed (FT) EXAFS spectra of Mn_1/CeO_2 and Mn foil as reference. Colour code: Oxygen, red; Cerium, yellow; Manganese, purple.

https://doi.org/10.1038/s41467-025-55838-6

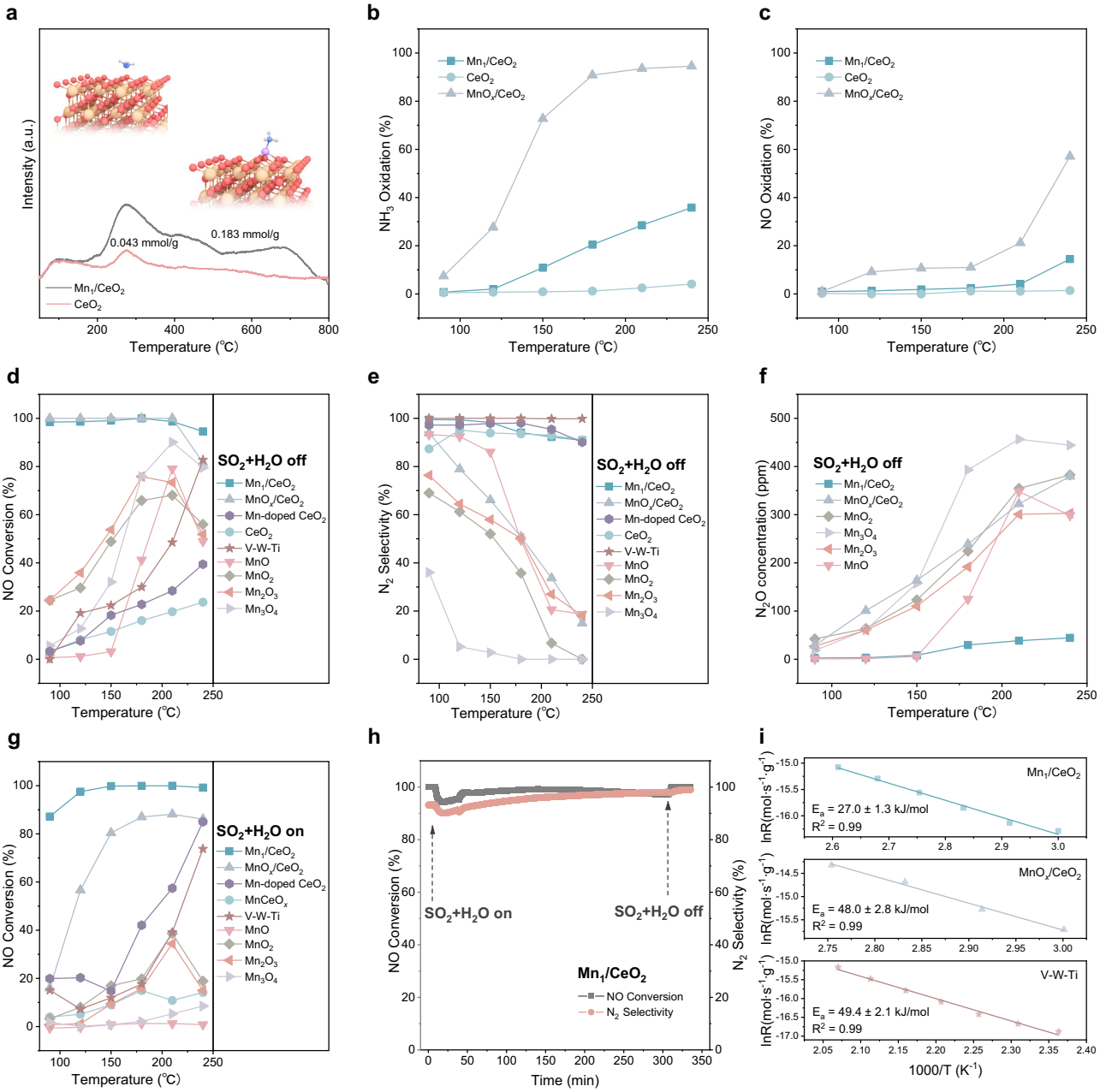

Fig. 4 | Catalytic performance of Mn_1/CeO_2 for NO_x removal. a NH_3-temperature programmed desorption (TPD) curve. Colour code: Nitrogen, blue; Oxygen, red; Hydrogen, white; Cerium, yellow; Manganese, purple. a. u. arbitrary units. **b** NH_3 oxidation (reaction conditions: $[NH_3] = 500$ ppm, $[O_2] = 5$ vol%). **c** NO oxidation (reaction conditions: $[NO] = 500$ ppm, $[O_2] = 5$ vol%). **d**–**f** NO conversion, N_2 selectivity and N_2O production for all the catalysts (reaction conditions: $[NH_3] = [NO] = 500$ ppm, $[O_2] = 5$ vol%). **g** NO conversion for all the catalysts (reaction conditions: $[NH_3] = [NO] = 500$ ppm, $[O_2] = 5$ vol%, $[H_2O] = 0$ vol%, $[SO_2] = 100$ ppm). Corresponding N_2 selectivity data is presented in Fig. S41. **h** Effect of H_2O and SO_2 at 180 °C on the NH_3-SCR performance of Mn_1/CeO_2. (Reaction conditions: $[NH_3] = [NO] = 50$ ppm, $[O_2] = 5$ vol%, $[H_2O] = 0$ or 10 vol%, $[SO_2] = 0$ or 100 ppm). **i** Kinetic analysis of the catalysts during the NH_3-SCR reaction (further details can be found in the Methods section).

maintained N_2O concentrations below 40 ppm during NH_3-SCR, highlighting their superior ability to minimize unwanted byproducts.

Given that SO_2 and H_2O in exhaust gases from stationary and mobile sources can lead to catalyst poisoning in practical applications, we also evaluated the catalytic performance of these catalysts in the presence of 10 vol% H_2O and 100 ppm SO_2 (Figs. 4g and S41). Despite a slight decrease in activity at 90 °C, Mn_1/CeO_2 maintained over 97% NO conversion and more than 95% N_2 selectivity in the 120–240 °C range. In contrast, the performance of MnO_x/CeO_2, Mn-doped CeO_2, and MnO_x catalysts significantly deteriorated upon exposure to SO_2 and H_2O. For example, NO conversion for MnO, MnO_2, Mn_2O_3, and Mn_3O_4 catalysts fell below 40% within the 90–240 °C range, indicating that the active sites on these MnO_x catalysts were severely poisoned by SO_2 and water vapor. Similarly, Mn-doped CeO_2, MnO_x/CeO_2, and V-W-Ti catalysts exhibited poor NO conversion, with values below 60% within the 90–210 °C range. The $MnCeO_x$ series of catalysts, despite achieving relatively high activity at 180 °C in the absence of SO_2 and H_2O (Fig. S42a), failed to sustain their activity when exposed to SO_2 and H_2O, highlighting the inability of traditional $MnCeO_x$ catalysts to effectively catalyze NO_x removal in the sulfur stream. In contrast, Mn_1/CeO_2 demonstrated remarkable stability, maintaining NO conversion above 90% and N_2 selectivity exceeding 90% after 300 min of testing at

https://doi.org/10.1038/s41467-025-55838-6

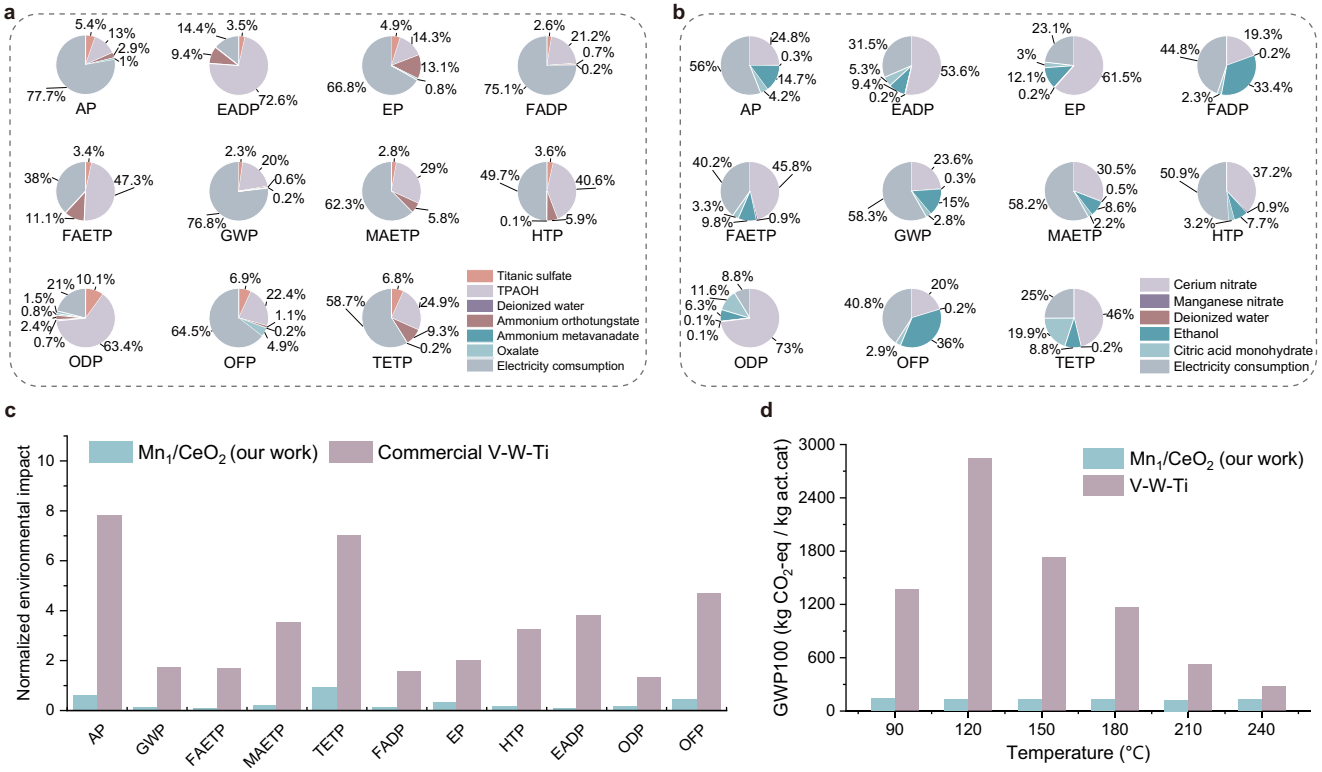

Fig. 5 | Environmental impact of Mn_1/CeO_2 production. a–b Distribution of LCA impacts in the catalyst production for commercialized V-W-Ti catalysts (**a**) and Mn_1/CeO_2 (**b**). **c** Environmental impacts comparison for two types of active catalysts. It is based on 11 sustainability indicators: acidification, global warming potential, freshwater aquatic ecotoxicity, marine aquatic ecotoxicity, terrestrial ecotoxicity, abiotic depletion potential for fossil fuels, eutrophication, human toxicity, abiotic depletion potential for elements, ozone layer depletion, and photochemical oxidation. The reported values are normalized per 1 kg of active catalyst. **d** Global warming potential (GWP100) of different catalysts at different temperatures.

180 °C in the presence of H_2O and SO_2 (Fig. 4h). Overall, traditional Mn-based catalysts tend to suffer from sulfate formation, which severely inhibits catalytic activity over time. Our results demonstrate that Mn_1/CeO_2 can effectively survive the sulfur stream, as supported by additional experiments and discussions provided in Supplementary Note 3 and Figs. S43–S47. For instance, TG-IR-MS experiments verified that no sulfate was formed on Mn_1/CeO_2 after the reaction. Given that sulfate formation is a widely observed phenomenon in most SCR catalysts with moderate redox properties, we further provided a detailed explanation of how Mn_1/CeO_2 suppresses SO_2 adsorption and oxidation, thereby preventing sulfate formation.

To further evaluate the intrinsic activity of Mn_1/CeO_2, MnO_x/CeO_2, and V-W-Ti in the NH_3-SCR reaction, kinetic studies were conducted. As shown in Fig. 4i, Mn_1/CeO_2 exhibited a significantly lower apparent activation energy (E_a) of 27 kJ·mol^{-1} compared to MnO_x/CeO_2 (48 kJ·mol^{-1}) and V-W-Ti (49.3 kJ·mol^{-1}). This indicates that Mn_1/CeO_2 are more efficient in catalyzing the NH_3-SCR reaction for NO reduction. Moreover, the design principles of T-SACs can be extended to other metals and catalytic processes, for example, enabling the selective hydrogenation of specific bonds in organic molecules with multiple unsaturation, thus achieving both high catalytic activity and product selectivity (Fig. S48 and Supplementary Note 4).

Environmental viability of T-SACs production

Early-stage lifecycle assessments (LCA) can effectively bridge the molecular and process levels to rigorously quantify the impact of different catalytic systems by accounting for emissions and waste embodied in all reaction components. These metrics help determine the degree to which novel technologies are environmentally sustainable and identify critical hotspots that warrant focused research efforts. In order to assess the environmental benefits of the Mn_1/CeO_2, a comprehensive cradle-to-gate LCA was performed in comparison to commercially available V-W-Ti catalysts for NH_3-SCR reactions. This assessment was based on their SCR activity and selectivity data under conditions that included the presence of SO_2 and H_2O. Distribution of LCA impacts in the catalyst production and Sankey diagram of embodied GWP flows are shown in Figs. 5a, b and S49. The LCA results reveal that the Mn_1/CeO_2 possess an environmental footprint that is an order of magnitude lower than that of commercially available V-W-Ti catalysts, as illustrated in Fig. 5c.

This significant reduction in environmental impact is primarily due to the exceptional performance of the Mn_1/CeO_2, which not only exhibits high conversion and selectivity, but also maintain these properties at lower temperatures. Figure 5d presents the Global Warming Potential (GWP100) of the two catalysts at different reaction temperatures, corresponding to their catalytic activities shown in Fig. 4g. The conventional V-W-Ti catalyst maintains a relatively high GWP100, which gradually decreases as the reaction temperature increases. In contrast, the Mn_1/CeO_2 consistently exhibits a significantly lower GWP100 across the entire temperature range, reflecting a substantially reduced carbon footprint. This stable performance under varying thermal conditions highlights the potential of Mn_1/CeO_2 to offer a more environmentally friendly alternative in processes where temperature fluctuations are common.

Mechanistic studies

In-situ Raman and DFT calculations show that during SCR pretreatment process (following H_2 purging), axially adsorbed oxygen atoms on Mn single atoms can be readily removed to form H_2O, thereby releasing the Mn sites (see Fig. S50). In-situ NAP-XPS at 240 °C during NH_3-SCR reveals that introducing Mn single atoms on CeO_2 increases the Ce^{3+}/Ce^{4+} ratio from 11% to 26%, indicating partial

https://doi.org/10.1038/s41467-025-55838-6

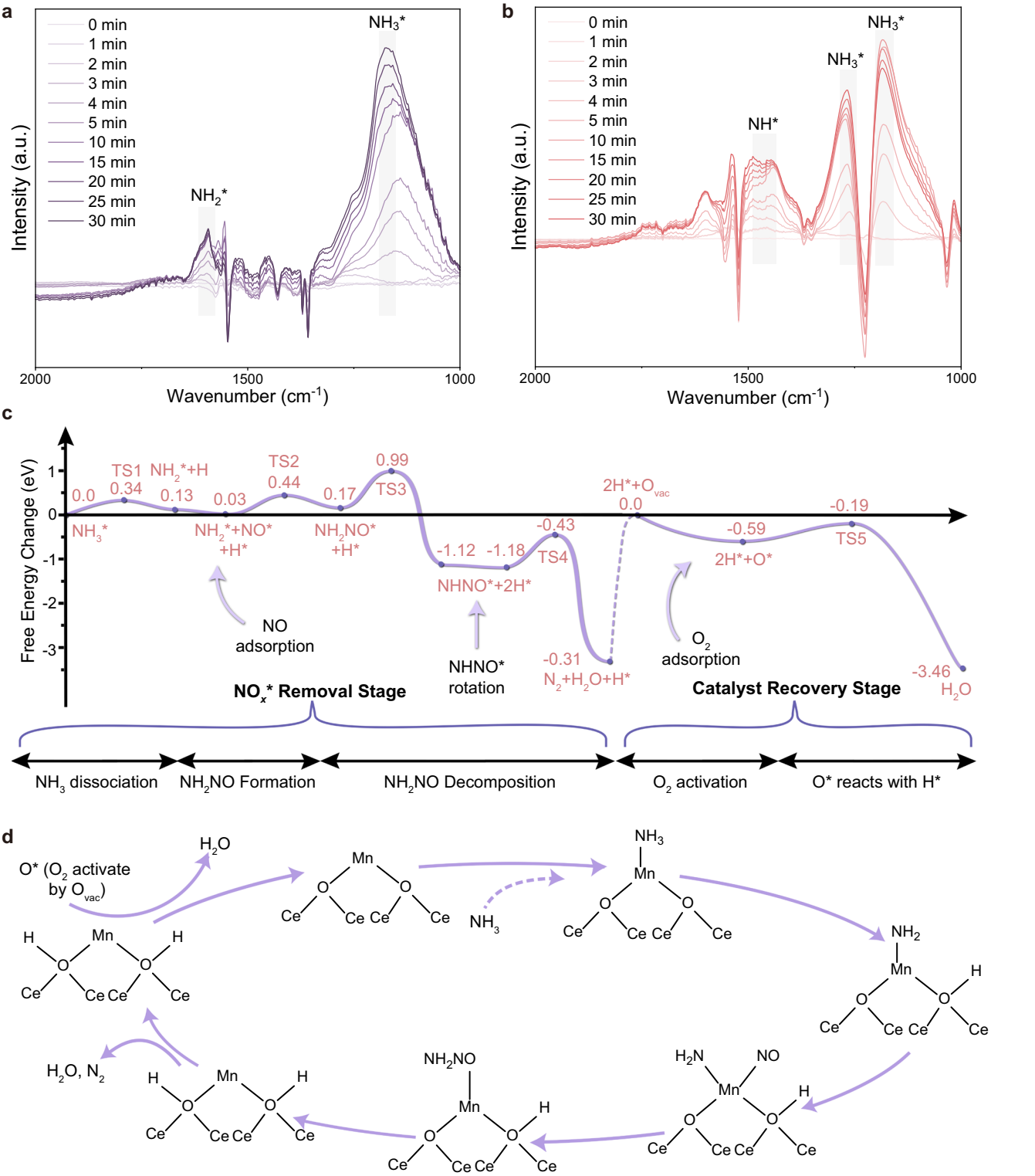

Fig. 6 | Proposed reaction mechanisms of NH_3-SCR for Mn_1/CeO_2. a In situ DRIFT spectra recorded at 210 °C while exposed to NH_3 for 30 min, along with vibrational peaks calculated by DFT. a. u. arbitrary units. **b** In situ DRIFT spectra recorded at 210 °C while exposed to NH_3, along with vibrational peaks calculated by DFT. a. u. arbitrary units. **c**, **d** Free-energy diagrams ($T = 500$ K) of reaction pathways for the NH_3 activation, NH_2NO formation, NH_2NO decomposition and H^* removal at Mn_1/CeO_2 surfaces.

reduction of Ce^{4+} to Ce^{3+} (Fig. S51a). The peak at 641.2 eV (Fig. S51b) confirms Mn single atoms as Mn^{2+}[44], stable in the SCR environment. In situ DRIFT spectra were conducted on Mn_1/CeO_2 T-SACs and MnO_x/CeO_2 catalysts to capture the NH_3 activation state during the reaction. As shown in Fig. 6a, b, IR bands at ~1100–1300 cm^{-1}, corresponding to NH_3 adsorption on Lewis acid sites[45–47], appear on both catalysts after 2 min. Additionally, an IR band at 1420–1470 cm^{-1}, assigned to NH species according to literature[45,48–52], is detected on MnO_x/CeO_2. MnO_x/CeO_2 samples also show an N-H stretching band at 3250 cm^{-1}[53,54] (Fig. S52), consistent with DFT-calculated harmonic

vibrational frequencies for NH adsorbed on MnO_x (Figs. S52 and 53). The DRIFT spectra of NH_3 adsorption on Mn_1/CeO_2 differ significantly from those on MnO_x/CeO_2. As adsorption progresses, bands in the range of 1550–1580 cm^{-1}, attributed to NH_2^* species[47,55,56], are enhanced, while NH^* species are scarcely detectable. This suggests that while MnO_x promotes NH_3 dissociation to NH, Mn_1/CeO_2 favors the oxidation of NH_3 to NH_2 and effectively prevents further oxidation to NH. DFT calculations further support these findings, confirming the correlation between IR bands and the vibrational modes of the adsorbed species (Supplementary Note 5). This underscores the catalyst's ability to facilitate the desired conversion of NH_3 to NH_2 while inhibiting unwanted side reactions from NH_2 to NH.

Comprehensive DFT calculations were further conducted to explore the catalytic mechanism in the NH_3-SCR reaction. The choice of the slab model for Mn_1/CeO_2 was informed by XAFS spectroscopy data, as shown in Fig. S54. Comparing adsorption free energies for NO, NH_3, and O_2 on both the pristine CeO_2 catalyst (Fig. S55) and Mn_1/CeO_2 (Fig. S56) illustrates that the incorporation of a single Mn atom significantly improves the binding of reactant molecules. The NH_3-SCR mechanism (Figs. 6c, d and S57) begins with NH_3 adsorption at the Mn single-atom site, forming NH_2^* with a hydrogen atom transferring to a nearby lattice O site, forming O-H^* species. The activation of NH_3 by Mn_1/CeO_2 has a reaction free energy change of 0.13 eV and a kinetic barrier of 0.34 eV, much lower than the 1.77 eV barrier on pure CeO_2 (Fig. S58). The activation of NH_3 by MnO_2 and Mn_3O_4 presents kinetic barriers of 0.62 eV (Fig. S59) and 0.72 eV (Fig. S60), respectively.

The kinetic barrier for NH_2^* oxidation to NH^* on Mn_1/CeO_2 is 3.3 eV (Fig. S5), much higher than for MnO_2 and Mn_3O_4. NO can then adsorb at the Mn site, forming NH_2NO^* via the Langmuir–Hinshelwood mechanism with a low activation barrier of 0.41 eV (TS2, Fig. 6c). The direct isomerization of NH_2NO^* to NHNOH faces a high barrier of 1.79 eV (Fig. S61), making it less likely. Mn_1/CeO_2 facilitates the dehydrogenation of NH_2NO^* to $NHNO^*$, which then decomposes into N_2 and H_2O with a low barrier of 0.75 eV (TS4). The formation of N_2O from $NHNO^*$ on Mn_1/CeO_2 is less favorable, requiring 0.34 eV and facing a high barrier of 1.56 eV (Fig. S62). H^* removal by lattice oxygen species is unlikely due to a high barrier of 1.13 eV (Fig. S63). Instead, H^* is removed through O_2 activation by an oxygen vacancy (O_{vac}) on Mn_1/CeO_2[57]. The energy required to form O_{vac} on Mn_1/CeO_2 is lower than on pure CeO_2 (2.62 eV vs. 2.93 eV, Fig. S64), suggesting Mn enhances O_{vac} formation on CeO_2. O_2 adsorbs at O_{vac}, forming O^*, which reacts with two adjacent H atoms to produce H_2O ($2H^* + O^*$, Fig. 6c). The activation energy for this pathway is 0.40 eV (TS5, Fig. 6c). DFT calculations also explored competing pathways, specifically the N-N coupling reaction via NH_4^+ and NO_2^- (Fig. S65). The formation of NH_4NO_2 on the Mn_1/CeO_2 surface was found to be highly endothermic (+2.87 eV), making this pathway less favorable. Additionally, it is well-established that Mn-based catalysts are prone to forming ammonium nitrite and nitrate, which are common causes of catalyst deactivation due to ammonium nitrate poisoning. To experimentally validate our computational findings regarding the suppression of NH_4NO_2 formation by Mn_1/CeO_2, we conducted supplementary experiments confirming that Mn_1/CeO_2 does not lead to the formation of ammonium nitrate during the SCR reaction. Detailed experimental evidence and discussion are provided in Supplementary Note 3 and Figs. S43–S47. This analysis clarifies the atomic-level catalytic mechanism of Mn_1/CeO_2 in the SCR process.

Discussion

This work creates an innovative design concept of T-SACs featuring metal single atoms in asymmetric patterns, whose spatial and electronic configurations form a protective barrier on the support surface, thereby preventing direct interactions with reactants associated with these atoms. LCA analysis quantifying the environmental benefits of the Mn_1/CeO_2 over traditional V-W-Ti catalyst shows a much lower carbon footprint in several recognized metrics. In-situ analysis and DFT studies highlight the strategic topological arrangement creates steric hindrance and electronic shielding effects around the isolated Mn center, significantly reducing NH_3 over-oxidation and thus enhancing N_2 selectivity. The development of single-atom topological catalysts not only broadens the scope of catalytic chemistry, but also opens new avenues for designing materials with tailored properties for specific applications, ushering in a new era of catalytic science where precision and efficiency are paramount.

Methods

Synthesis of Mn_1/CeO_2

A typical synthesis process is as follows: a precursor solution was prepared by dissolving 8 g of glycerol and 24 g of citric acid in a mixture of 400 mL deionized water and 400 mL ethanol. This solution was stirred continuously for at least 2 h to ensure complete dissolution and homogeneity. Subsequently, 24 g cerous nitrate hexahydrate ($Ce(NO_3)_3{\cdot}6H_2O$) and 2 g manganese nitrate solution (50 wt% aqueous solutions of $Mn(NO_3)_2$) were added to the homogeneous solution, followed by stirring at 600 rpm for another 2 h. The mixture was then heated to 80 °C to evaporate the solvent, leading to the formation of a gel-like precursor. The resulting gel-like precursor was thoroughly ground into a fine powder, placed in a sealed container, and then subjected to calcination at 150 °C for 6 h in an oven (first annealing step, see Figs. S66 and 67). The calcined powder was subsequently ball-milled for at least 2 h to ensure uniformity. The milled sample was then annealed in a reducing atmosphere of N_2/H_2 (4 vol% H_2 and 96 vol% N_2) at 250 °C for 2 h (second annealing step), followed by multiple repetitions of the ball-milling and annealing process. Finally, the resulting solid powder was subjected to annealing in a tubular furnace at 600 °C under an N_2 atmosphere for 4 h, followed by calcination in a muffle furnace at 300 °C for 3 h (third annealing step). For kilogram-scale production, the synthesis was scaled up by 2000 times through proportional scaling of both reactants and reaction vessel volume.

The synthesis of other metal T-SACs (Fe, Ru, Zn) follows the same steps, using the corresponding metal precursors and adjusting the annealing temperatures accordingly. The decomposition temperatures of the respective metal citrates were obtained from thermogravimetric analysis curves, which were used to confirm the temperature for each annealing step.

Synthesis of MnO_x/CeO_2

As shown in Fig. S26a, a precursor solution was prepared by dissolving 8 g of glycerol and 24 g of citric acid in a mixture of 400 mL deionized water and 400 mL ethanol. This solution was stirred continuously for at least 2 h to ensure complete dissolution and homogeneity. Subsequently, 24 g cerous nitrate hexahydrate ($Ce(NO_3)_3{\cdot}6H_2O$) and 2 g manganese nitrate solution (50 wt% aqueous solutions of $Mn(NO_3)_2$) were added to the homogeneous solution, followed by stirring at 600 rpm for another 2 h. The mixture was then heated to 80 °C to evaporate the solvent, forming a gel-like precursor. This gel was then annealed in a tubular furnace at 800 °C under an N_2 atmosphere for 4 h, followed by calcination in a muffle furnace at 300 °C for 3 h.

Synthesis of CeO_2

In the synthesis of the CeO_2 catalyst, manganese nitrate was not added; the other synthesis steps remained the same as for Mn_1/CeO_2.

Synthesis of Mn-doped CeO_2

As shown in Fig. S26b, Glucose (3.94 g) was dissolved in 160 mL of deionized water with magnetic stirring for approximately 60 min. Acrylamide (2.13 g), cerous nitrate hexahydrate ($Ce(NO_3)_3{\cdot}6H_2O$), and manganese nitrate solution (50 wt% aqueous solutions of $Mn(NO_3)_2$) were then added to form a transparent solution. The pH of the solution was adjusted to 10 by adding 6 mL of ammonia solution (25–28 wt%)

dropwise while stirring. This addition caused the solution to transition into a stiff gel. The gel mixture was stirred for an additional 6 h and then transferred to a 200 mL Teflon-lined autoclave. The autoclave was sealed and heated in an oven at 180 °C for 72 h. After the reaction, the autoclave was allowed to cool naturally to room temperature. The resulting orange suspension and precipitate were separated by centrifugation. The suspension was washed three times with deionized water and ethanol, and then dried at 80 °C for approximately 24 h. The dried precipitate was calcined under N_2 atmosphere with a flow rate of 5 mL/min in a tube furnace at 600 °C for 6 h. Finally, the calcined product was further treated in a muffle furnace at 400 °C for 4 h under an air atmosphere.

Synthesis of $MnCeO_x$ and $MnCeO_x$-2

As shown in Fig. S26d, $MnCeO_x$ catalysts were prepared by a standard co-precipitation method from aqueous solutions of nitrates similar to that used by Gongshin et al.[58]. First, 4.34 g cerous nitrate hexahydrate ($Ce(NO_3)_3{\cdot}6H_2O$) and 0.36 g manganese nitrate solution (50 wt% aqueous solutions of $Mn(NO_3)_2$) were dissolved in water. Then, an excess amount of ammonium carbonate solution was slowly added to the mixture while stirring continuously. The resulting mixture was aged for 1 h and subsequently filtered. The obtained solid sample was dried at 120 °C in air for 12 h and then calcined at 600 °C for 6 h. For the synthesis of $MnCeO_x$-2, the amount of manganese nitrate solution was increased to 1.432 g, and the calcination temperature was raised to 650 °C in a muffle furnace.

Synthesis of MnO, Mn_3O_4, Mn_2O_3 and MnO_2

MnO was prepared by first synthesizing Mn_3O_4 through a hydrothermal method and then subjecting it to H_2 reduction[59]. Initially, 0.353 g of manganese acetylacetonate was dissolved in 40 mL of absolute ethanol. The solution was then transferred into an 80 mL Teflon-lined autoclave and heated at 120 °C for 10 h. After heating, the mixture was washed three times with ethanol and once with deionized water through centrifugal separation. The resulting powder (Mn_3O_4) was collected after freeze-drying for 12 h. Finally, the Mn_3O_4 powder was thermally treated at 600 °C for 2 h in a tube furnace under a reducing gas flow (5 vol% H_2 and 95 vol% argon) with a heating rate of 5 °C/min, yielding the final MnO catalyst.

As shown in Fig. S26c, MnO_2, Mn_3O_4, and Mn_2O_3 catalysts were prepared using a hydrothermal synthesis method similar to that described by Leilei et al. [60]. First, 0.118 g of $KMnO_4$ and 0.6 mL ethylene glycol (EG) were dispersed in 44 mL distilled water. The mixed solution was stirred for 5 h and then transferred into a 50 mL Teflon-lined stainless-steel autoclave. The autoclave was sealed and heated at 120 °C for 10 h, then allowed to cool naturally to room temperature. The products (c-MnOOH) were collected by centrifugation, washed several times with ethanol and distilled water to remove excess reactants and byproducts, and then dried in a vacuum at 50 °C for 12 h. MnO_2 were prepared by treating c-MnOOH at 400 °C for 4 h in air. Mn_2O_3 and Mn_3O_4 were obtained by calcining c-MnOOH at 700 °C for 5 h in air and argon atmosphere, respectively.

Synthesis of V-W-Ti

V_2O_5-WO_3/TiO_2 catalysts (denoted as V-W-Ti) were synthesized using the classical impregnation method. Ammonium metatungstate ($(NH_4)_{10}H_2W_{12}O_{42}{\cdot}4H_2O$) was used as the precursor for WO_3. To prepare the impregnation solution, 0.404 g of ammonium metatungstate was dissolved in 100 mL of deionized water in a beaker. In a separate beaker, 0.07 g of ammonium metavanadate (NH_4VO_3) and 0.151 g of oxalic acid ($C_2H_2O_4$) (used as a solubilizing agent for vanadium, at twice the molar amount of vanadium) were dissolved in 100 mL of deionized water. The solutions were then combined and stirred at 60 °C for 30 min until complete dissolution (the solution should turn deep blue, with no crystalline particles remaining at the bottom). The prepared ammonium metavanadate and ammonium metatungstate solution was then gradually titrated onto 5 g of TiO_2 powder using a pipette. The mixture was stirred thoroughly to ensure uniform distribution of the solution onto the TiO_2 powder, followed by ultrasonic treatment for 30 min to enhance mixing. After allowing the mixture to stand for 2 h, it was dried in a conventional oven at 100 °C for at least 12 h with adequate ventilation. The dried precursor was then calcined in a muffle furnace at 600 °C for 5 h. Following the calcination, the catalyst was allowed to cool naturally to room temperature, resulting in the formation of the V-W-Ti catalyst.

NO_x removal catalytic activity measurement

The self-designed and built fixed-bed reactor was used to test the performance of the catalyst for NH_3-SCR reaction, including the catalytic activity and N_2 selectivity of the catalyst. The reaction device is shown in Fig. S68. First, the prepared catalyst powder was pressed into tablets, sieved to 60–100 mesh, placed in a reaction tube (8 mm inner diameter), and then a thermocouple was inserted into the reaction tube to detect the reaction temperature. The gas concentration of the reaction gas was adjusted by a flow meter. The reaction gas comprised 500 ppm NO, 500 ppm NH_3, 5 vol% O_2, 100 ppm SO_2 (when used) and 10 vol% H_2O (when used), and the balance gas was N_2 or Ar. The reaction space velocity (GHSV) was set to 50,000 h^{-1} or 100,000 h^{-1} according to the actual sample and experimental settings. The weight of a typical catalyst is provided in Table S11. When the reaction reached a stable state, the gas concentrations (NO, NO_2, N_2O, and NH_3) in the inlet and outlet streams were measured using an infrared gas analyzer (GASMET FTIR DX4000). The SCR performance was evaluated across a temperature range of 90 °C to 300 °C, with NO conversion and N_2 selectivity calculated using Eq. (1) and Eq. (2). NH_3 and NO oxidation rates were determined using Eq. (4) and Eq. (5), respectively.

$$NO\ conversion = \frac{[NO_x]_{inlet} - [NO_x]_{outlet}}{[NO_x]_{inlet}} \times 100\% \tag{1}$$

$$NO_x = NO + NO_2 \tag{2}$$

$$N_2\ selectivity = 1 - \frac{2 \times [N_2O]_{outlet}}{[NO_x]_{inlet} + [NH_3]_{inlet} - [NO_x]_{outlet} - [NH_3]_{outlet}} \times 100\% \tag{3}$$

$$NH_3\ oxidation = \frac{[NH_3]_{inlet} - [NH_3]_{outlet}}{[NH_3]_{inlet}} \times 100\% \tag{4}$$

$$NO\ oxidation = \frac{[NO_2]_{outlet}}{[NO]_{inlet}} \times 100\% \tag{5}$$

For the kinetic studies of the NH_3-SCR reaction, the gas composition was consistent with that of the standard SCR reaction, and a gas hourly space velocity (GHSV) of approximately 150,000 h^{-1} was employed. Reaction rates (r) were normalized to the catalyst mass using Eq. (6), and activation energies (E_a) were calculated using the Arrhenius Eq. (7).

$$r = \frac{F_{NOx} \cdot X_{NOx}}{W_{cat}} \tag{6}$$

$$r = [NO_x]_0 A e\left(-\frac{E_a}{RT}\right) \tag{7}$$

In these calculations, F_{NO_x} represents the NO_x flow rate (mol/s), X_{NO_x} is the NO_x conversion, W_{cat} is the catalyst mass (g), and $[NO_x]_0$

denotes the initial NO_x concentration, encompassing NO, NO_2, or a mixture of both.

Catalyst characterization

We characterized the crystal phase, morphology, and microstructure of the samples by XRD (Rigaku Dmax-2400, RIGAKU, Japan, Cu Kα radiation, 40 kV, 40 mA). The surface characteristics of single-atom catalysts were studied by aberration-corrected (AC) high-angle annular dark-field (HAADF) STEM and sub-angstrom-scale resolution was realized. The AC-HAADF-STEM images in this article were all obtained using a Titan Cubed Themis G2 300 spherical AC scanning transmission electron microscope at the Electron Microscopy Laboratory of Peking University. The X-ray absorption spectrum was obtained at the 1W1B-XAFS experimental station of the Beijing Synchrotron Radiation Facility. Athena software was used for data processing. NH_3-TPD experiments were performed on automatic chemical adsorption analyzers (ChemBET Pulsar TPR/TPD, Quantachrome Instruments, USA and AUTOCHEM II 2920, USA).

We obtained in situ DRIFTS from an FT-IR spectrophotometer (Nicolet 6700, Thermo Fisher, US) by accumulating 32 scans with a resolution of 4 cm^{-1}. For in situ Raman measurements, a 532 nm laser was used for excitation. We recorded the Raman spectra on a Horiba LaRAM HR Evolution (Horiba Jobin Yvon) with a resolution of 5 cm^{-1}. Furthermore, we performed in situ NAP-XPS measurements on a SPECS NAP-XPS system, and XPS spectra were obtained using monochromatized Al Kα irradiation (1486.6 eV) generated by an Al anode (SPECS XR-50) and an excitation source power fixed at 50 W. In situ NAP-XPS measurements at pressures up to 25 mbar were possible because of a differential pumping system, which separated the electron analyzer (SPECS Phoibos NAP-150) from the reaction area.

The TG-FTIR-MS experiment was conducted using Perkin Elmer instruments: TGA 8000 thermogravimetric analyzer, FRONTIER FTIR spectrometer, and Clarus SQ8T mass spectrometer. Samples were heated from 30 °C to 900 °C at 20 °C/min under nitrogen flow (50 mL/min for balance and 20 mL/min for purge gas) in a corundum crucible. Transfer lines and interfaces were maintained at 280 °C, with an effluent gas flow of 50 mL/min. FTIR detection used a DTGS detector with 8 cm^{-1} resolution, and MS operated at 230 °C with an m/z range of 35–300. FTIR and MS detections were synchronized with the TGA program.

DFT methods

Plane-wave DFT calculations were performed in the Vienna Ab-initio Simulation Package (VASP)[61–63] code in our study. With a kinetic energy cutoff of 600 eV, the projector augmented wave (PAW)[64] scheme was employed to simulate the atoms' potentials. We used Perdew-Burke-Ernzerhof (PBE)[65] generalized gradient approximation functional for all calculations. A Hubbard U value (U_{eff} = U−J, J = 0) of 4.5 eV and 3.5 eV[66–68] were added to the PBE functional to describe the localized electrons on the 4*f* orbitals of Ce and the 3*d* orbitals of Mn. Optimized structures were obtained by minimizing the forces on each ion using the conjugate gradient algorithm until the forces were below 0.02 eV/Å. We set the convergence criterion for the total energies of the investigated systems to 10^{-6} eV. LOBSTER program was employed to calculate COHP to analysis bonding states[69].

For a certain reaction (A→B), the reaction free-energy ΔG [including the DFT total energy, zero-point energy, vibrational enthalpy (thermal corrections), and vibrational entropy (at T = 500 K)] is defined as follows:

$$\Delta G = G_B - G_A \tag{8}$$

We employed the CINEB method[70] with a force tolerance of 0.02 eV/Å to calculate kinetic barriers. We further verified the optimized TS structures by which only having a single imaginary frequency. The kinetic barrier (E_a) was calculated as the energy difference between the TS and the IS.

We used a slab model (15.21 Å × 13.17 Å × 30.72 Å) to simulate the CeO_2 (111) surface, which is a nine-layer slab containing 48 Ce and 96 O atoms, separated by a vacuum space of 21.51 Å. Furthermore, the top six atomic layers and surface species were allowed to relax, while the bottom three layers remained fixed in their bulk position. We implemented a capping strategy that involved using pseudo-hydrogen (pseudo-H) atoms[71] to prevent the occurrence of dangling bonds.

The Mn_1/CeO_2 catalyst model was constructed by placing a Mn single atom on the CeO_2 (111) surface. All possible sites were selected and optimized to obtain the most stable Mn_1/CeO_2 configuration based on the principle of lowest energy. The crystal plane model of MnO_2 was a periodic slab model of the supercell constructed by cutting along the (211) plane on the MnO_2 primitive cell. The supercell size of the simulated MnO_2 (211) surface was 13.95 Å × 11.76 Å × 24 Å. Contains 72 Mn and 96 O atoms. The crystal plane model of Mn_3O_4 was a periodic plate model of the supercell constructed by cutting along the (101) plane on the MnO_2 primitive cell. The supercell size of the simulated MnO_2 (101) surface is 16.11 Å × 15.98 Å × 24 Å. Contains 48 Mn and 96 O atoms.

AIMD methods

All AIMD simulations were conducted using the VASP to investigate the dissociation process of NH_2 and the formation of Mn single atoms on the CeO_2 surface. The details of the AIMD calculations largely align with those described in the DFT methods section, with some adjustments made to the computational approach to reduce computational costs, as outlined below.

The wave functions were expanded with a cutoff energy of 400 eV and the Gaussian smearing with a width of 0.2 eV was employed. No spin polarization is considered to reduce the computational cost because it has almost no impact on the overall energies[72–75]. Two layers of CeO_2 (111) facets were cleaved, incorporating a vacuum layer of 25 Å, to construct the surface structures. Additionally, one manganese salt (either MnCA or $MnCl_2$, used for simulating the Mn single atom formation process) or NH_2 (for simulating the NH_2 dissociation process) was introduced into the slab model.

Firstly, the model has been fully relaxed with the energy convergence criterion of 10^{-4} eV and the force convergence criterion of 0.02 eV/Å, respectively. Only the Γ point has been used in the Brillouin zone since the model is large.

To simulate the formation process of single atoms and the dehydrogenation steps of NH_2, as well as to calculate their activation free energy barriers, we employed the slow-growth sampling approach within the constrained molecular dynamics framework. Below, we present an illustrative example that details the simulation specifics of synthesizing Mn single atoms. This process utilizes the constrained AIMD method within our synthesis strategy.

The optimized model has been heated up from 0 K to 523 K by velocity scaling over 2615 fs every MD step and equilibrated at 523 K for 1 ps with a 1-fs time step. Finally, the constrained AIMD has been used with slow-growth method to simulate the dynamic process. The collective variable is the combination of the distance between the atom in manganese salt and CeO_2. All collective variables increase with 0.0005 Å per MD step. Besides, to verify the stability of Mn-single atom on CeO_2 surface, the CeO_2 surface with three Mn-atoms have been built. After optimization, the model has been heated up from 0 K to 1073 K by velocity scaling over 5365 fs every MD step and equilibrated at 1073 K for 10 ps. The energy of all process has been counted every MD step and smoothed using Savitzky-Golay method per 1000 points.

LCA methods

This investigation conducts a life cycle assessment (LCA) of Mn_1/CeO_2 catalysts alongside commercially available V-W-Ti catalysts, utilizing

1 kg of the active catalyst as the functional unit for comparison. The LCA follows the CML baseline[76] analytical framework, employing eChemstore® Intelligence software for its execution. This assessment rigorously adheres to the four distinct phases of LCA as delineated in the ISO 14040/14044 standards[77]. The activity and emission factor data employed in this life cycle assessment are derived from a combination of experimental findings, scholarly literature, and the ecoinvent 3.9 database. For any materials not cataloged in the ecoinvent 3.9 database, this study meticulously retraces the preparation process of these materials to the point where the raw materials are identifiable and locatable within the database.

Data availability

Relevant data supporting the key findings of this study are available within the article and the Supplementary Information file. All raw data generated during this study are available from the corresponding authors upon request.

References

1. Zaera, F. Designing sites in heterogeneous catalysis: are we reaching selectivities competitive with those of homogeneous catalysts? *Chem. Rev.* **122**, 8594–8757 (2022).
2. Sun, G.-Q. et al. Electrochemical reactor dictates site selectivity in N-heteroarene carboxylations. *Nature* **615**, 67–72 (2023).
3. Fu, X. et al. Medium entropy alloy wavy nanowires as highly effective and selective alcohol oxidation reaction catalysts for energy-saving hydrogen production and alcohol upgrade. *Ees. Catal.* **2**, 1285–1292 (2024).
4. Wang, X. et al. Discovery of promising Cu-based catalysts for selective propane dehydrogenation to propylene assisted by high-throughput computations. *J. Catal.* **438**, 115718 (2024).
5. Inomata, Y. et al. Bulk tungsten-substituted vanadium oxide for low-temperature NOx removal in the presence of water. *Nat. Commun.* **12**, 557 (2021).
6. Song, I. et al. Simple physical mixing of zeolite prevents sulfur deactivation of vanadia catalysts for NO_x removal. *Nat. Commun.* **12**, 901 (2021).
7. Chen, W., Zou, R. & Wang, X. Toward an atomic-level understanding of the catalytic mechanism of selective catalytic reduction of NO_x with NH_3. *ACS Catal.* **12**, 14347–14375 (2022).
8. Han, L. et al. Selective catalytic reduction of NO_x with NH_3 by using novel catalysts state of the art and future prospects. *Chem. Rev.* **119**, 10916–10976 (2019).
9. Voigt, C. et al. Nitrous oxide emissions from permafrost-affected soils. *Nat. Rev. Earth Environ.* **1**, 420–434 (2020).
10. Shi, S. et al. Selective hydrogenation via precise hydrogen bond interactions on catalytic scaffolds. *Nat. Commun.* **14**, 429 (2023).
11. Lan, X. & Wang, T. Highly selective catalysts for the hydrogenation of unsaturated aldehydes: a review. *ACS Catal.* **10**, 2764–2790 (2020).
12. Li, C. et al. Selective hydroboration of unsaturated bonds by an easily accessible heterotopic cobalt catalyst. *Nat. Commun.* **12**, 3813 (2021).
13. Frei, M. S. et al. Nanostructure of nickel-promoted indium oxide catalysts drives selectivity in CO2 hydrogenation. *Nat. Commun.* **12**, 1960 (2021).
14. Vanni, M. et al. Selectivity control in palladium-catalyzed CH_2Br_2 hydrodebromination on carbon-based materials by nuclearity and support engineering. *ACS Catal.* **13**, 5828–5840 (2023).
15. Veenstra, F. L. P., Ackerl, N., Martín, A. J. & Pérez-Ramírez, J. Laser-microstructured copper reveals selectivity patterns in the electrocatalytic reduction of CO_2. *Chem* **6**, 1707–1722 (2020).
16. Wan, C. et al. Amorphous nickel hydroxide shell tailors local chemical environment on platinum surface for alkaline hydrogen evolution reaction. *Nat. Mater.* **22**, 1022–1029 (2023).
17. Zhao, X. & Liu, Y. Origin of selective production of hydrogen peroxide by electrochemical oxygen reduction. *J. Am. Chem. Soc.* **143**, 9423–9428 (2021).
18. Davis, H. J. & Phipps, R. J. Harnessing non-covalent interactions to exert control over regioselectivity and site-selectivity in catalytic reactions. *Chem. Sci.* **8**, 864–877 (2017).
19. Mahatthananchai, J., Dumas, A. M. & Bode, J. W. Catalytic selective synthesis. *Angew. Chem. Int. Ed.* **51**, 10954–10990 (2012).
20. Bai, X. et al. Dynamic stability of copper single-atom catalysts under working conditions. *J. Am. Chem. Soc.* **144**, 17140–17148 (2022).
21. Yu, S., Levell, Z., Jiang, Z., Zhao, X. & Liu, Y. What is the rate-limiting step of oxygen reduction reaction on Fe–N–C catalysts? *J. Am. Chem. Soc.* **145**, 25352–25356 (2023).
22. Prasoon, A. et al. Site-selective chemical reactions by on-water surface sequential assembly. *Nat. Commun.* **14**, 8313 (2023).
23. Pang, S. H., Schoenbaum, C. A., Schwartz, D. K. & Medlin, J. W. Directing reaction pathways by catalyst active-site selection using self-assembled monolayers. *Nat. Commun.* **4**, 2448 (2013).
24. Qing, Y., Tamagaki-Asahina, H., Ionescu, S. A., Liu, M. D. & Bayley, H. Catalytic site-selective substrate processing within a tubular nanoreactor. *Nat. Nanotechnol.* **14**, 1135–1142 (2019).
25. Mitchell, S. & Pérez-Ramírez, J. Single atom catalysis: a decade of stunning progress and the promise for a bright future. *Nat. Commun.* **11**, 4302 (2020).
26. Qiao, B. et al. Single-atom catalysis of CO oxidation using Pt_1/FeO_x. *Nat. Chem.* **3**, 634–641 (2011).
27. Xu, H., Cheng, D., Cao, D. & Zeng, X. C. Revisiting the universal principle for the rational design of single-atom electrocatalysts. *Nat. Catal.* **7**, 207–218 (2024).
28. Zhang, S. et al. Atomically dispersed bimetallic Fe-Co electrocatalysts for green production of ammonia. *Nat. Sustain.* **6**, 169–179 (2023).
29. Guo, X. et al. Direct, nonoxidative conversion of methane to ethylene, aromatics, and hydrogen. *Science* **344**, 616–619 (2014).
30. Cao, L. et al. Atomically dispersed iron hydroxide anchored on Pt for preferential oxidation of CO in H_2. *Nature* **565**, 631–635 (2019).
31. Hai, X. et al. Geminal-atom catalysis for cross-coupling. *Nature* **622**, 754–760 (2023).
32. Hai, X. et al. Scalable two-step annealing method for preparing ultra-high-density single-atom catalyst libraries. *Nat. Nanotechnol.* **17**, 174–181 (2022).
33. Lang, R. et al. Single-atom catalysts based on the metal–oxide interaction. *Chem. Rev.* **120**, 11986–12043 (2020).
34. Han, L. et al. A single-atom library for guided monometallic and concentration-complex multimetallic designs. *Nat. Mater.* **21**, 681–688 (2022).
35. Xie, S. et al. Pt Atomic single-layer catalyst embedded in defect-enriched ceria for efficient CO oxidation. *J. Am. Chem. Soc.* **144**, 21255–21266 (2022).
36. Merte, L. R. et al. CO-induced embedding of Pt adatoms in a partially reduced FeO_x film on Pt (111). *J. Am. Chem. Soc.* **133**, 10692–10695 (2011).
37. Yu, J. et al. Highly stable Pt/CeO_2 catalyst with embedding structure toward water-gas shift reaction. *J. Am. Chem. Soc.* **146**, 1071–1080 (2024).
38. Kim, C. H., Qi, G., Dahlberg, K. & Li, W. Strontium-doped perovskites rival platinum catalysts for treating NO_x in simulated diesel exhaust. *Science* **327**, 1624–1627 (2010).
39. Becher, J. et al. Chemical gradients in automotive Cu-SSZ-13 catalysts for NO_x removal revealed by operando X-ray spectro-tomography. *Nat. Catal.* **4**, 46–53 (2021).
40. Shindell, D. et al. Climate, health, agricultural and economic impacts of tighter vehicle-emission standards. *Nat. Clim. Chang.* **1**, 59–66 (2011).

41. Chaudhary, E. et al. Reducing the burden of anaemia in Indian women of reproductive age with clean-air targets. *Nat. Sustain.* **5**, 939–946 (2022).
42. Krishna, S. H. et al. Influence of framework Al density in chabazite zeolites on copper ion mobility and reactivity during NO_x selective catalytic reduction with NH_3. *Nat. Catal.* **6**, 276–285 (2023).
43. Liu, C., Shi, J.-W., Gao, C. & Niu, C. Manganese oxide-based catalysts for low-temperature selective catalytic reduction of NO_x with NH_3: A review. *Appl. Catal. A-Gen.* **522**, 54–69 (2016).
44. Wang, Y. et al. Synergistic effect of N-decorated and Mn^{2+} doped ZnO nanofibers with enhanced photocatalytic activity. *Sci. Rep.* **6**, 32711 (2016).
45. Hu, W. et al. Mechanistic investigation of NH_3 oxidation over V-0.5Ce$(SO_4)_2$/Ti NH_3-SCR catalyst. *Catal. Commun.* **112**, 1–4 (2018).
46. Jin, R. et al. The role of cerium in the improved SO_2 tolerance for NO reduction with NH_3 over Mn-Ce/TiO_2 catalyst at low temperature. *Appl. Catal. B-Environ.* **148**, 582–588 (2014).
47. Liu, Y. et al. DRIFT studies on the selectivity promotion mechanism of Ca-modified Ce-Mn/TiO_2 catalysts for low-temperature NO reduction with NH_3. *J. Phys. Chem. C.* **116**, 16582–16592 (2012).
48. Busca, G., Lietti, L., Ramis, G. & Berti, F. Chemical and mechanistic aspects of the selective catalytic reduction of NO_x by ammonia over oxide catalysts: a review. *Appl. Catal. B-Environ.* **18**, 1–36 (1998).
49. Suárez, S., Jung, S. M., Avila, P., Grange, P. & Blanco, J. Influence of NH_3 and NO oxidation on the SCR reaction mechanism on copper/nickel and vanadium oxide catalysts supported on alumina and titania. *Catal. Today* **75**, 331–338 (2002).
50. Slavinskaya, E. M. et al. Studies of the mechanism of ammonia oxidation into nitrous oxide over Mn-Bi-O/α-Al_2O_3 catalyst. *J. Catal.* **222**, 129–142 (2004).
51. Peña, D. A., Uphade, B. S., Reddy, E. P. & Smirniotis, P. G. Identification of surface species on titania-supported manganese, chromium, and copper oxide low-temperature SCR catalysts. *J. Phys. Chem. B* **108**, 9927–9936 (2004).
52. Liang, H., Gui, K. & Zha, X. DRIFTS study of γFe_2O_3 nano-catalyst for low-temperature selective catalytic reduction of NO_x with NH_3. *Can. J. Chem. Eng.* **94**, 1668–1675 (2016).
53. Krueger, P. J. Fundamental NH_2 stretching frequencies in amines and amides. *Nature* **194**, 1077–1078 (1962).
54. Wilfong, W. C., Srikanth, C. S. & Chuang, S. S. C. In situ ATR and DRIFTS studies of the nature of adsorbed CO_2 on tetraethylenepentamine films. *ACS Appl. Mater. Inter.* **6**, 13617–13626 (2014).
55. Chen, Y. et al. Promoting effect of Nd on the reduction of NO with NH_3 over CeO_2 supported by activated semi-coke: an in situ DRIFTS study. *Catal. Sci. Technol.* **5**, 2251–2259 (2015).
56. Qi, G. & Yang, R. T. Characterization and FTIR studies of MnO_x-CeO_2 catalyst for low-temperature selective catalytic reduction of NO with NH_3. *J. Phys. Chem. B* **108**, 15738–15747 (2004).
57. Chen, W., Wang, X. & Xu, S. Investigation of intrinsic catalytic mechanism for NO oxidation to NO_2 in CeO_2 used for NO removal. *Chem. Eng. J.* **460**, 141801 (2023).
58. Qi, G., Yang, R. T. & Chang, R. MnO_x-CeO_2 mixed oxides prepared by co-precipitation for selective catalytic reduction of NO with NH_3 at low temperatures. *Appl. Catal. B-Environ.* **51**, 93–106 (2004).
59. Tian, H. et al. In situ electrochemical Mn(III)/Mn(IV) generation of Mn(II)O electrocatalysts for high-performance oxygen reduction. *Nano-Micro Lett.* **12**, 161 (2020).
60. Lan, L., Li, Q., Gu, G., Zhang, H. & Liu, B. Hydrothermal synthesis of γ-MnOOH nanorods and their conversion to MnO2, Mn2O3, and Mn3O4 nanorods. *J. Alloy. Compd.* **644**, 430–437 (2015).
61. Kresse, G. & Furthmüller, J. Efficient iterative schemes for ab initio total-energy calculations using a plane-wave basis set. *Phys. Rev. B* **54**, 11169–11186 (1996).
62. Kresse, G. & Furthmüller, J. Efficiency of ab-initio total energy calculations for metals and semiconductors using a plane-wave basis set. *Comp. Mater. Sci.* **6**, 15–50 (1996).
63. Kresse, G. & Hafner, J. Ab initio molecular dynamics for open-shell transition metals. *Phys. Rev. B-Condens Matter* **48**, 13115–13118 (1993).
64. Blöchl, P. E. Projector augmented-wave method. *Phys. Rev. B* **50**, 17953–17979 (1994).
65. Perdew, J. P., Burke, K. & Ernzerhof, M. Generalized gradient approximation made simple. *Phys. Rev. Lett.* **77**, 3865–3868 (1996).
66. Kildgaard, J. V., Hansen, H. A. & Vegge, T. DFT + U study of strain-engineered CO_2 reduction on a CeO_2–x (111) facet. *J. Phys. Chem. C.* **125**, 14221–14227 (2021).
67. Wu, T., Deng, Q., Hansen, H. A. & Vegge, T. Mechanism of water splitting on gadolinium-doped CeO_2(111): A DFT + U study. *J. Phys. Chem. C.* **123**, 5507–5517 (2019).
68. Su, Y.-Q., Liu, J.-X., Filot, I. A. W., Zhang, L. & Hensen, E. J. M. Highly active and stable CH_4 oxidation by substitution of Ce^{4+} by two Pd^{2+} ions in CeO_2(111). *ACS Catal.* **8**, 6552–6559 (2018).
69. Maintz, S., Deringer, V. L., Tchougréeff, A. L. & Dronskowski, R. LOBSTER: a tool to extract chemical bonding from plane-wave based DFT. *J. Comput. Chem.* **37**, 1030–1035 (2016).
70. Henkelman, G., Uberuaga, B. P. & Jónsson, H. A climbing image nudged elastic band method for finding saddle points and minimum energy paths. *J. Chem. Phys.* **113**, 9901–9904 (2000).
71. Xu, S. & Carter, E. A. CO_2 Photoelectrochemical reduction catalyzed by a GaP(001) photoelectrode. *ACS Catal.* **11**, 1233–1241 (2021).
72. Cheng, T., Wang, L., Merinov, B. V. & Goddard, W. A. III Explanation of dramatic pH-dependence of hydrogen binding on noble metal electrode: Greatly weakened water adsorption at high pH. *J. Am. Chem. Soc.* **140**, 7787–7790 (2018).
73. Li, P., Huang, J., Hu, Y. & Chen, S. Establishment of the potential of zero charge of metals in aqueous solutions: different faces of water revealed by Ab initio molecular dynamics simulations. *J. Phys. Chem. C.* **125**, 3972–3979 (2021).
74. Li, C.-Y. et al. In situ probing electrified interfacial water structures at atomically flat surfaces. *Nat. Mater.* **18**, 697–701 (2019).
75. Li, P. et al. Revealing the role of double-layer microenvironments in pH-dependent oxygen reduction activity over metal-nitrogen-carbon catalysts. *Nat. Commun.* **14**, 6936 (2023).
76. Guinée, J. B. *Handbook on Life Cycle Assessment: Operational Guide to the ISO Standards*, Vol. 7 (Springer Science & Business Media, 2002).
77. Standardization, I. O. F. *Environmental Management: Life Cycle Assessment; Requirements and Guidelines*, Vol. 14044 (ISO Geneva, Switzerland, 2006).

Acknowledgements

This work was financially supported by the National Natural Science Foundation of China (52332007Z) and the NRF, Prime Minister's Office, Singapore, under the Competitive Research Program Award (NRF-CRP29-2022-0004L). The authors would like to acknowledge the support from the AI for Science (AI4S) Preferred Program at Peking University Shenzhen Graduate School, China. The DFT calculations were supported by Shanxi Supercomputing Center of China (TianHe–2), High-Performance Computing Platform of Peking University. The authors also acknowledge the Beijing Beilong Super Cloud Computing Co., Ltd for providing HPC resources that have contributed to the research results reported in this paper. We thank the Materials Processing and Analysis Center, Peking University, and the Beijing Synchrotron Radiation Facility (BSRF) at beamline 1W1B for their support in material characterization.

Author contributions

J. Lu and R. Zou supervised the project and organized the collaboration. W. Chen and M. Bao designed the experiments and synthesized the

materials. W. Chen and B. Ma conceived the reaction mechanism and carried out quantum-chemical calculations. M. Bao and L. Feng discovered the catalytic activity. X. Zhang and S. Gao conducted the comparison studies and synthetic applications. S. Xi performed the XAFS measurement and structural analysis. F. Meng and Z. Qiu performed the electron microscopy experiments and data analysis. R. Zhong advised on the experiments, methodologies and data presentation. W. Chen wrote the draft, with the assistance of X. Hai. All authors discussed the results and edited and commented on the manuscript.

Competing interests
The authors declare no competing interests.

Additional information
Supplementary information The online version contains supplementary material available at https://doi.org/10.1038/s41467-025-55838-6.

Correspondence and requests for materials should be addressed to Xiao Hai, Jiong Lu or Ruqiang Zou.

Peer review information *Nature Communications* thanks Yaqiong Su, and the other, anonymous, reviewer(s) for their contribution to the peer review of this work. A peer review file is available.